Published in Materials Science and Engineering A, 627 (2015) 10-20

Strengthening of an Al-Cu-Mg alloy processed by high-pressure torsion due to clusters, defects and defect-cluster complexes

Ying Chen[a], Nong Gao[a*], Gang Sha[b,c], S.P. Ringer[b], Marco J. Starink[a]

[a] Engineering Materials, Faculty of Engineering and the Environment, University of Southampton, SO17 1BJ, UK

[b] Australian Centre for Microscopy & Microanalysis, The University of Sydney, Madsen Building F09, NSW 2006, Australia

[c] Herbert Gleiter Institute of Nanoscience, Nanjing University of Science and Technology, Nanjing 210094, China

*Corresponsing Aouthor email: N.Gao@soton.ac.uk

Abstract

A physically-based model is established to predict the strength of cluster strengthened ultrafine-grained ternary alloys processed by severe plastic deformation. The model incorporates strengthening due to dislocations, grain refinement, co-clusters (due to short range order and modulus strengthening) and solute segregation. The model is applied to predict strengthening in an Al-Cu-Mg alloy processed by high-pressure torsion (HPT). The microstructure was investigated using transmission electron microscopy (TEM), atom probe tomography (APT), and X-ray diffraction (XRD). Analysis of XRD line profile broadening shows that the dislocation density increases significantly due to severe plastic deformation, which contributes to the increase of strength. APT reveals the presence of nanoscale co-clusters and defect-solute clustering. The concepts of the multiple local interaction energies between solutes and dislocations were used to quantitatively explain the strengthening

mechanisms. The model shows a good correspondence with measured microstructure data and measured strength.

Key words: High-pressure torsion; Strengthening mechanism; Modelling; Atom probe tomography (APT); Cluster-dislocation interaction

1. Introduction

Ultrafine-gained (UFG) metallic materials produced by severe plastic deformation (SPD) have garnered an intense scientific interest because strengths of these materials are significantly increased without significant changes in overall sample dimension and alloy composition [1]. The research has revealed that the hardness increase in metals due to SPD is strongly material-dependent; the hardness increase in pure Al is very low (~15 HV for high purity Al, [2]), while those in Al alloys are higher (i.e. ~30 HV to ~120 HV [2-7]). For engineering applications UFG alloys are more attractive than the pure metals because of their higher microstructural stability [8-10], better mechanical properties and their wider range of properties. To exploit the benefits of UFG alloys processed by SPD, it is crucial to understand the mechanisms of multiple hardening and the formation of solute-defect nanostructures during SPD processing.

Dislocation hardening models developed by Ashby [11], Hansen et al [12], Estrin et al [13, 14] and Starink et al [15, 16], describe deformation from low strain to ultra-high strain. Initially a very high dislocation density is introduced, which in many metals and alloys leads to the formation of an intragranular structure consisting of cells with thick cell walls and low angles of misorientation. As the strain increases, the cell wall thickness decreases and they evolve into grain boundaries (which are high-angle non-equilibrium and construct ultrafine grains [17]). However, apart from the partly empirical analysis by Starink and co-workers [15, 16], the multiple strengthening by dissolved atoms in UFG alloys has been rarely studied.

On the other hand, during the past 15 years a number of studies on conventionally processed heat-treatable ternary Al alloys (i.e. particularly in Al-Cu-Mg alloys [18-21] and Al-Mg-Si alloys [22-24]) have revealed the existence of nanoscale co-clusters which can be as small as ~0.3 nm. It has been shown that in several underaged alloys these co-clusters are the dominant strengthening factor, with short range order strengthening being the dominant strengthening mechanism [20, 24]. Solute behaviours in ultrafine-grained/nanograined Al alloys after SPD processing have been studied with the aid of atom probe tomography in a number of alloys [25-29]. These investigations have shown that pre-existing precipitates can be fragmented and partially dissolved (i.e. in Al-Cu [30-33], Al-Cu-Mg [34]), whilst solute atoms can be redistributed and segregated to grain boundaries/dislocations (e.g. in AA7075 (Al-Zn-Mg-Cu) [25], AA6060 [26], AA6061 [27], AA7136 [28]). Studies of equilibrium grain boundary segregation on nanograined materials indicate that solute segregation reduces the grain boundary energy and stabilizes of crystalline defects [35, 36]. Although the general trend of segregation of solutes to grain boundaries and dislocations segregation has been predicted in thermodynamic models [8, 37-39], the calculations have not been used to predict material mechanical properties. Our study provides an analysis aimed at understanding the effect of solute segregation to grain/subgrain boundaries (dislocation walls) and dislocations on strengthening, in particular for the ultrafine-grained microstructures processed by HPT. The present research was conducted on Al-Cu-Mg discs processed by HPT at room temperature. The samples were investigated by transmission electron microscopy (TEM), atom probe tomography (APT), and X-ray diffraction (XRD) line broadening analysis. The main aim of the present work is to derive a model to predict strength increase in the SPD processing, in particular, the effect of solute co-clusters and solute-defect clusters. The new model will employ some of the concepts from the models and papers reviewed above, and will be tested against the microstructure data.

2. A physically based model

2.1 General model structure

The yield strength of a polycrystalline metal is related to the critically resolved shear stress (CRSS) of the grains and the grain boundary strengthening, with an expression of the type (e.g. [16, 40-42]):

$$\sigma = \Delta\sigma_{gb} + M\Delta\tau_{tot} \quad (1)$$

$\Delta\sigma_{gb}$ is the yield strength increment due to the grain boundaries; M is an orientation factor (often termed the Taylor factor), which is related to texture and the orientation of the tensile axis relative the main axes of the worked specimen [40, 41]; $\Delta\tau_{tot}$ is the CRSS of the grains. We will consider the various strengthening mechanisms in the below.

2.2 Critically resolved shear stress of the grains

Within a grain in a ternary (or higher order) alloy that has been work-hardened, $\Delta\tau_{tot}$ is determined by a range of mechanisms and nanoscale features. Within these grains, the resistance against deformation (i.e. resistance against the movement of dislocations) is due to the interaction of the moving dislocations with obstacles in the form of other dislocations (primarily those introduced by the prior work hardening), various types of clusters, precipitates and solute atoms. If we consider a ternary heat treatable aluminium alloy (for instance an Al-Mg-Cu alloy), atoms of type A (for instance Mg) and type B (for instance Cu) dissolve in a lattice of host metal M (the fcc Al-rich phase) after solution heat treatment, and on low temperature ageing some (or most) of the solutes can form clusters. Fig. 1(a) illustrates how a dislocation moving on a slip plane encounters co-clusters, including a 2-atom co-cluster and 4-atom co-clusters intersecting the slip plane (see also [20, 24, 43]). Fig. 1(b) illustrates this from a different orientation (looking down onto a slip plane), now with

also a small number of stationary dislocations present (resulting from a small amount of prior deformation). This shows the moving dislocation will pass through the co-clusters and dislocations. On passing of one dislocation through the A-B co-cluster, the A-B bonds will be destroyed and some will be retained [20]. After SPD processing, a large number of dislocations are stored in the grain, as illustrated in Fig. 1(c).

In the present model five contributions to CRSS of grains will be considered: the intrinsic CRSS, $\Delta\tau_0$; the contribution due to dislocations, $\Delta\tau_d$; the contribution due to solid solution strengthening, $\Delta\tau_{ss}$; the contribution due to co-clusters $\Delta\tau_{cl}$, which involves a short range order strengthening component, $\Delta\tau_{SRO}$, and a modulus strengthening component, $\Delta\tau_m$. Here, a linear approximation of the superposition of these five contributions is used [15, 16, 41, 44]:

$$\Delta\tau = \Delta\tau_0 + \Delta\tau_d + \Delta\tau_{ss} + \left(\Delta\tau_{SRO} + \Delta\tau_m\right) \quad (2)$$

The intrinsic strength of pure Al ($\Delta\tau_0$) is very low, and to account for the small contributions of Mn, Fe and Si impurities, here 10 MPa is taken for $\Delta\tau_0$ [40, 41].

The increment of CRSS is due to both statistically stored dislocations (SSDs) and geometrically necessary dislocations (GNDs) and is given by [15, 45].

$$\Delta\tau_d = \alpha_1 Gb\sqrt{\rho_T} = \alpha_1 Gb\sqrt{\rho_{SSD} + \rho_{GND}} \quad (3)$$

where α_1 is an empirical constant ranging from 0.2-0.5 [46], in aluminium alloys this value is usually taken as 0.3 [16], which is applied in the present model. G is the shear modulus (taken as 26 GPa), b is the Burgers vector.

The increment in CRSS due to solid solution strengthening $\Delta\tau_{ss}$ is described by [40, 47]

$$\Delta\tau_{ss} = \Sigma k_j c_j^n \quad (4)$$

where k_j are the factors describing the strengthening due to the individual elements and c_j are the concentrations of the alloying elements in solid solution and n is a constant (see Ref [47-49]). We will here adopt n=1 as used in [24]. In the present alloys in the naturally aged and

SPD processed conditions, solid solution strengthening has a relatively small contribution to the overall strength (typically 0.5 to 1%) [20][24].

The co-cluster strengthening is taken to be due to short range order strengthening and modulus hardening where the former is the dominant effect in typical Al alloys [20, 24]. The work done in deforming the lattice through movement of dislocations hampered by co-clusters equals the change in energy related to short range order per unit area on slip planes in Al matrix [20, 50], i.e.:

$$\Delta\tau_{\mathrm{SRO}} = \frac{\gamma_{\mathrm{SRO}}}{b} \tag{5}$$

where γ_{SRO} is the change in energy per unit area on slip planes on the passing of one dislocation. Ref. [20] provides a detailed calculation on the change in area density of A-B nearest neighbour bonds crossing the slip plane on passing of one dislocation, which is simplified as

$$\rho_{A-B}\left(n_d=0\right)-\rho_{A-B}\left(n_d=1\right)=\frac{4}{\sqrt{3}b^2}\frac{2}{3}\left(y_A+y_B\right) \tag{6}$$

where $\rho_{\mathrm{A\text{-}B}}$ (n_d=0) and $\rho_{\mathrm{A\text{-}B}}$ (n_d=1) are the area density of A-B nearest neighbour bonds crossing the slip plane {111} before and after passage of one dislocation; y_{A} and y_{B} are the amount of A and B atoms in the co-clusters, respectively. Although further dislocation movement will cause further changes in density of clusters, the first dislocation experiences the greatest resistance due to clusters [20, 24]. Hence, the short range order strengthening due to co-clusters can be approximated as [20]:

$$\Delta\tau_{SRO}=\frac{\gamma_{\mathrm{SRO}}}{b}=\frac{\Delta H_{\mathrm{A\text{-}B}}}{b}\left[\rho_{\mathrm{A\text{-}B}}(n_d=0)-\rho_{\mathrm{A\text{-}B}}(n_d=1)\right]=C\frac{\Delta H_{A-B}}{b^3}\left(y_A+y_B\right) \tag{7}$$

where $\Delta H_{\mathrm{A\text{-}B}}$ is the enthalpy of the nearest neighbour bond. (For more detailed descript of the derivation of the latter equation the reader is referred to [20].) Clusters possess an elastic modulus that is different to the matrix which will result in an additional strengthening

mechanism. This modulus strengthening mechanism is difficult to deal with in theory but simplified treatment has been developed in a range of works [20, 24, 51]. The CRSS due to difference in shear modulus is approximated as

$$\Delta\tau_m = \frac{\Delta\mu}{4\pi\sqrt{2}} f^{\frac{1}{2}} \tag{8}$$

$$\mu_{\mathrm{cl}} = \frac{m\mu_M + a\mu_A + b\mu_B}{m+a+b} \tag{9}$$

where f is the volume fraction of the clusters, $\Delta\mu$ is the difference in shear modulus between surrounding metallic phase and clusters, with the average cluster ($M_mA_aB_b$) modulus, μ_{cl}, expressed as a weighted average of the pure substances in Eq. (9) [20]. The cluster average modulus is 29.6 GPa (using μ_{Al}=26.2 GPa, μ_{Cu}=48.3 GPa, μ_{Mg}=17.3 GPa from [52], with compositions given in the same reference), providing $\Delta\mu$ = 3.4 GPa.

2.3 Strengthening due to grain refinement

In recent works [53, 54], a power-law dependence of yield or flow stress on grain size was expressed as follows

$$\sigma = \sigma_{\mathrm{o}} + k_{\mathrm{HP}} d^{-x} \tag{10}$$

where d is the grain size, σ_{o} and k_{HP} are material constant, the exponents are reported to be in the range from 0 to1 for different classes of materials [53, 54]. Analysis of data for a number of metals and alloys has revealed that the typical values of exponent x range from 0.6 to 1 for fcc metals, whilst they are around 0.5 or less for bcc metals, and 0.2 or even zero for ceramics [55]. To date, there is no theory fully explaining such experimental exponents. Taylor forest hardening [56] gives x=1/2, which has been applied by a large number of strengthening behaviours in coarse-grained metals in the traditional Hall-Petch relation [57]. On the other hand, theory based on the fundamental physics of yield and plastic deformation by dislocations [58, 59] implies a exponent of 1, which provides

$$\Delta\sigma = \frac{k}{d} \tag{11}$$

where the value of k is correlated to intrinsic materials factors [11, 15, 16], in general proportional to shear module and Burgers vector, Gb. Hence:

$$\Delta\sigma_{gb} = \alpha_2 Gb\left(\frac{1}{d}\right) \tag{12}$$

where α_2 is a constant, d is the grain size.

2.4 Hardness/ strength ratio of deformed Al alloys

The relation between Vickers hardness and strength (yield strength or flow stress) can often be approximated through [60]:

$$\sigma = \frac{HV}{C} \tag{13}$$

where C is a constant, which is usually taken as ~3, see e.g. [16, 42, 61, 62]. In particular the flow stress at plastic strain of 8% has been associated with C=3. In SPD processed metals and alloys that strengthen as a result of SPD, the work-hardening ability of materials decreases strongly with increasing deformation, and the yield strength σ_y is approximately equal to σ_{UTS} [62]. In our assessment of the strengthening model we can thus take yield strengths from Vickers hardness test as σ_y = HV/ 3, where the unit HV is MPa. But we should take into account that prior to SPD our Al-Cu-Mg alloy does have a strong work hardening, and HV_{T351}/3 is 467 MPa, which substantially exceeds the σ_y of the alloy. Thus for very low deformations the above approximation will have a reduced accuracy.

It is noted that for the indentation depth obtained with the load used in the present work, the indention size effect is too small to influence the measurements in a significant manner [63].

3. Methodology

AA2024-T351 (Al-2.1Cu-1.8Mg-0.08Si at.% with limited Mn and Fe) samples were processed by high pressure torsion (HPT) at room temperature. Prior to HPT, the samples were cut to discs 9.8 mm in diameter and mechanically ground and polished to a thickness of 0.83 to 0.85 mm. The HPT processing was conducted on a facility with two anvils with a depression of 0.25 mm each in depth and 10 mm in diameter. The samples were held in the depression. The volume of a whole disk is larger than the total volume of depression in both anvils, so there is at least some limited outward flow between the upper and lower anvils [1], i.e. it is quasi-constrained. In order to reduce the friction between the upper and lower anvil, a lubricant of MoS_2 was placed around the edges of both depressions. The samples were pressed at a pressure of 6GPa and torsion-strained at a rotation speed of 1 rotation per minute. The samples were deformed by HPT for 1/8 rotation (1/8r-HPT), 1/4 rotation (1/4r-HPT), 1 rotation (1r-HPT), 3 rotations (3r-HPT), 5 rotations (5r-HPT), and 16 rotations (16r-HPT). Following HPT the samples were stored at room temperature (RT) for several weeks.

Following HPT, the disks were carefully ground up to 4000-grit SiC paper and polished to a mirror-like surface with a 0.05 μm colloidal silica suspension and 0.1 μm diamond paste. The Vickers microhardness, Hv, was measured at 9 positions distributed at equal distances across lines through the centre, using a load of 500 g held for 15 s. The value of each distance from the centre was taken as the average value of 6 lines at positions with a same distance to the centre.

Samples for XRD were punched from HPT processed discs. XRD was performed on the peripheral rings (2.5 mm<r<5mm, where r is the distance to the centre). Subsequently, they are carefully ground up to 4000SiC paper and carefully two-step polished using 6 μm and 1 μm paste. XRD was conducted using Bruker D2 PHASER diffractometer equipped with a

graphite monochromator using Cu *K*α radiation. The experiments were performed at 50 steps per degree and a count time of 1s per step. In this experiment, the step size was chosen to satisfy the condition full width at half maximum (FWHM)/step size larger than 5 [64].

Transmission electron microscopy was conducted on 1/4r-HPT, 1r-HPT and 5r-HPT processed samples. The HPT processed discs were ground to a thickness of ~150 μm and subsequently TEM samples of 3 mm in diameter were punched out from the periphery (see Fig. 2). Subsequently, the samples were thinned in the centre using twin-jet electropolishing with an electrolyte solution of HNO_3: methanol=1:3 at -30 °C, and thus the electron transparent region was situated at about 3.5 mm from the centre of the original HPT disc. TEM samples were examined using a JEOL3010 microscope which was operated at 300 kV.

Three-dimensional atom probe was carried out under an ultrahigh vacuum ($\sim 1 \times 10^{-8}$ Pa) at ~20 K, using a local electrode atom probe (LEAP4000X Si®). UV laser pulsing energy was 40 *p*J at the pulse repetition rate of 200 kHz [65]. The detection efficiency of this instrument is about 55%. Reconstruction and visualization of atom probe tomography data was performed using the Imago Visualization and Analysis Software (IVAS^{TM}). In our Al-Mg-Cu alloy, Mg, Cu and Si atoms were identified as clustered/segregated if they had a separation distance of <0.6 nm. To detect small solute clusters, the smallest solute clusters taken into account were nominated to contain at least 2 solute atoms [66].

4. Results

4.1 Hardness of HPT-processed Al-Cu-Mg alloy

Due to the geometry of the HPT [1], strain is inhomogeneous and the equivalent (von Mises) strain increases with the distance to the centre, reaching the maximum value at the edge regions. Fig. 3 shows the distribution of the Vickers microhardness of HPT-deformed samples vs. distance from the centre of discs. The hardness of HPT-deformed samples is higher than that of as-obtained T351 samples. The hardness of HPT-deformed samples increases with distance from the centre of disk as well as the increasing numbers of rotations. 1/8r-HPT and 1/4r-HPT show a similar distribution of Vickers hardness, which is about 166 HV in the centre and 200~206 HV in the peripheral areas. The hardness of HPT discs in the peripheral regions is reasonably similar after 1, 3, 5 and 16 rotations, tending towards a saturation of 260 HV. In centre areas (distance to the centre< 2 mm) the hardness increases gradually with the number of rotations.

4.2 X-ray diffraction analysis

The X-ray diffraction patterns of the alloy deformed by HPT straining for ¼, 1, 3, 5 and 16 rotations are shown in Fig. 4. In each pattern, the main peaks are due to the fcc Al-rich phase. Compared to the pattern of the sample prior to HPT, the profiles of HPT-deformed samples have broadened. It is known that small grain size and internal microstrains are the two main sources contributing to X-ray line broadening [67], and the dislocation density ρ in peripheral ring areas can be calculated from the lattice microstrain, $<\varepsilon^2>^{1/2}$ [4, 68] by:

$$\rho = \frac{2\sqrt{3}\left\langle \varepsilon^2 \right\rangle^{\frac{1}{2}}}{D_c b} \tag{14}$$

where D_c is the average crystallite size (related to coherently scattering domains), which was measured using Rietveld refinement method and calculated using materials analysis diffraction (Maud) software; the dislocation density ρ should be regarded as an average value

over the volume studied. The uncertainties of the XRD quantitative calcuation have ben considered by the deviation between experiment data and refinement data.

We applied the Rietveld refinement method, in which all of the data points of a pattern were fitted to structure models, taking into account adjustable parameters of samples and instrumental effects, using the materials analysis diffraction (Maud) software [70-72]. The X-ray diffraction profiles of HPT samples were described by the pseudo-Voigt function [73] to fit the experimental data. The Pseudo-Voigt function takes the form:

$$I(2\theta) = I_{hkl}\left[\eta L\left(2\theta - 2\theta_1\right) + \left(1-\eta\right)G\left(2\theta - 2\theta_1\right)\right] \quad (15)$$

where $L(2\theta\text{-}2\theta_1)$ and $G(2\theta\text{-}2\theta_1)$ represent suitably normalised Lorentz and Gaussian functions, and η (the " Lorentz fraction") and (1- η) represent the fractions of each used [64]. The fitting to the measured XRD pattern is performed by a least-square calculation. The instrumental broadening and asymmetry as well as Gaussianity of reflections were evaluated using Caglioti et al's model [74] and programmed in Maud using the standard Al_2O_3 pattern preformed in the XRD instruments.

Examples of Rietveld full pattern fitting are illustrated in Fig. 5 for a 3r-HPT sample (a) and a 5r-HPT sample (b). The evolutions of dislocation density and crystallite size obtained through the Rietveld refinement are shown in Fig. 6. This figure reveals that the dislocation density increases significantly up to 2.6×10^{14} m^{-2} within an ¼ HPT turn and increase further to ~3.3×10^{14} m^{-2} for higher number of rotations. Using the Maud software, the crystallite size decreases to 65$\pm$ 5nm for 1/4r-HPT and further decreases to ~50 nm for higher rotations.

4.3 TEM

TEM micrographs obtained at positions at ~4 mm from the centre of disks after ¼r-HPT, 1r-HPT and 5r-HPT processing are shown in Fig. 7 (a)-(c), respectively. The average grain sizes were measured using the modified line intercept method described in [15]. The average line intercept grain sizes are 177±25 nm, 145±25 nm and 157±30 nm, respectively, after ¼r-HPT, 1r-HPT and 5r-HPT processing. There is very little difference in grain sizes in the outer regions of both disks. High dislocation densities within some of the ultrafine grains were observed in a 5r-HPT sample (Fig. 7 (c)).

4.4 APT

Fig. 8 (a)-(c) shows atom maps of Mg, Cu and Si for a sample processed by 1/4r HPT. The analysis volume contained only 2 sections of grain boundaries, here marked GB1 and GB2. Both Mg and Cu are seen to segregate at the grain boundaries (GBs). The total number density of solute clusters in the volume in Fig. 8 was identified as 1.90×10^{26} m^{-3}. Mg-Cu co-clusters were the dominant type of detected clusters, with density 1.06×10^{26} m^{-3}. Quantitative measurement of the composition profiles of GB1 in the 1/4r-HPT Al-Cu-Mg alloy is shown in Fig. 8 (e). It appears that peak Mg concentration of GB1 was 2.40 at% and peak Cu concentration was lower, ~1.90 at%.

The single element atom maps of the 5r-HPT sample in Fig. 9 (a)-(c), indicate that in this sample GBs only enriched with Cu and Si, with no clear segregation of Mg. This indicates that GB boundaries can have different segregation characteristic depending on the nature of each GB, i.e. disorientation angle of GBs, tilt and rotation components of the grain boundary et al (see also [26, 28]). The nearest-neighbour analysis in Fig. 9 (e) and (f) confirmed that Cu and Si developed non-random distributions slightly more strongly than Mg atoms, because of the clustering of Cu-Mg and Si-Mg, which segregated to GBs. The detected solute clusters

have an overall number density of 1.99×10^{26} m^{-3}, with Mg-Cu co-clusters being dominant with a number density of 1.07×10^{26} m^{-3} (see Table 1).

The overall number density of solute clusters increased slightly as the number of rotations increased. The average Mg/Cu ratio in clusters was around 1 after 1/4r-HPT, and it increased slightly to 1.15 after 5r-HPT processing.

5. Modelling results and further refinement of model

We applied the model described in Section 2 to predict the yield strengths of the samples, using the microstructure data in the Section 4 combined with data of constants and parameters available in the literature. The model parameters are provided in Table 2. In the model, we used the grain sizes determined by TEM, which for HPT samples were on average 3 times larger than the crystallite sizes obtained from XRD line broadening analysis. (For 3r-HPT and 16r-HPT no TEM data is available and the grain size was estimated as 3 times the measured crystallite size.) Dislocation densities were taken from the XRD line broadening analysis in Section 4.2. The amounts of Cu and Mg in the co-clusters y_{Cu} and y_{Mg} in the model are determined using the analysis of thermodynamics presented in [20]; i.e. the stoichiometry of the clusters is considered fixed such that $y_{Cu} : y_{Mg} = 1$. The analysis in [20] shows that that for the present Al-2.1Cu-1.8Mg-0.08Si at.% alloy, at the present low temperature ageing of the samples before and after HPT (all at room temperature), the Mg dissolved in the Al-rich phase (i.e. not forming clusters) is $3\text{x}10^{-3}$ at%, (which is virtually negligible) and its Cu content is 0.3 at%. The latter contributes to solid solution strengthening through $\Delta\tau_{ss}$ (Eq. (4)). The effective volume of the clusters as used in the modulus hardening is calculated using the approach described in [20].

The results of the model predictions are presented in Fig. 11 (green triangles). In this figure the predictions are compared with measured HV/3 (blue diamonds), with HV determined in the peripheral areas (distance to centre> 3 mm) was used. In all samples the cluster hardening is the main strengthening effect. The model broadly captures the trends, but the predicted yield strengths of HPT processed samples are about 150 MPa lower than strengths measured from Vickers hardness. Clearly the model in Section 2, which is based on non-interacting superposition of strengthening effects in cluster-hardened undeformed ternary alloys and classical work hardening through dislocations and grains boundaries, underestimates strength in the present HPT processed cluster-hardened alloy. (An analysis of potential inaccuracies introduced by input to the model and model parameters, such as ρ, k_{Mg}, k_{Cu}, M, suggests any deviations in model predictions due to these sources is less than 50 MPa.) To include interaction between HPT-induced defects and clusters we propose the below extension to the model.

The model in Section 2 effectively assumes that solute atoms and dislocations produce separate and distinct strengthening effects (see Fig. 1 (b) and 1 (c)). However, atomic probe analysis of samples subjected to 1/4r-HPT (Fig. 8) and 5r-HPT (Fig. 9) indicates solute clusters segregated to dislocations and grain boundaries, which can provide an additional strengthening mechanism. These dislocation-solute interactions can reduce the Gibbs free energy of the defect through decreasing the enthalpy associated with it see e.g. [37], producing a more stable state (see schematic illustration in Fig. 10). These dislocation-solute complexes will form a stronger barrier to movement of dislocations, through a mechanism that is similar to the cluster strengthening by short range order: when a dislocation passes through these solute-dislocation obstacles, it causes a higher enthalpy change. We may represent this here by modifying Eq. (7) as follows:

$$\Delta\tau_{SRO} = C\frac{\Delta H_{\text{A-B-dis}}}{b^3}(y_A + y_B) \tag{16}$$

where $\Delta H_{\text{A-B-dis}}$ is the average enthalpy of the various types of A-B-dislocation clusters:

$$\Delta H_{\text{A-B-dis}} = f_1 \Delta H_{\text{A-B}} + f_2 \Delta H_{\text{A-dis}} + f_3 \Delta H_{\text{B-dis}} + f_4 \Delta H_{(\text{A-B})_n\text{-dis}} \quad (17)$$

where f_1 to f_4 are the fraction of A-B cluster, fraction of A segregated to dislocations, fraction of B segregated to dislocations, and fraction of A-B co-clusters segregated to dislocations, respectively; $\Delta H_{\text{A-B}}$ is the enthalpy of A-B co-clusters in M matrix, $\Delta H_{\text{A-dis}}$, $\Delta H_{\text{B-dis}}$ the enthalpy of single atom A or B located at dislocations (disordered Al matrix), $\Delta H_{\text{(A-B)n-dis}}$ the enthalpy of co-clusters located at dislocations (disordered Al matrix). $\Delta H_{\text{A-B-dis}}$ increased as compared to $\Delta H_{\text{A-B}}$.

The latter modification has been employed by adjusting $\Delta H_{\text{A-B-dis}}$ to obtain the best possible fit between data and model. The results presented in Fig. 11 (red crosses) show an excellent correspondence with the measured HV/3 data for all samples over the range of HPT processing applied for 1 rotation or more. $\Delta H_{\text{A-B-dis}}$ in this fit is 50±5 kJ/mole, which compares to $\Delta H_{\text{Cu-Mg}}$ = 34.5 kJ/mole [20].

For ¼ rotation the fit with $\Delta H_{\text{A-B-dis}}$ = 50 kJ/mole overestimates the strength, and the model without cluster-dislocation complexes provides a good fit (i.e. with $\Delta H_{\text{Cu-Mg}}$ = 34.5 kJ/mole). Apparently, for these low deformations, the amount of dislocations present after HPT and the amount of dislocation movement during HPT is too low to allow the formation of significant cluster-dislocation complexes. Most of the Cu and Mg in the 1/4r-HPT sample then present in Cu-Mg clusters that are not related to HPT dislocations. In that sense the 1/4r-HPT sample is similar to the 2024-T351 sample.

6. Discussion

The model of cluster strengthening in the absence of clustering on defects which forms the basis of Section 2 provides an explanation for a range of observations in ternary and higher order alloys. For example, the strength of conventionally processed, coarse-grained,

underaged Al-Cu-Mg and Al-Mg-Si alloys were accurately presented by a model in which cluster strengthening is the dominant strengthening mechanism [20, 24]. However, the model cannot fully explain the strengthening in the present SPD-processed Al alloys, and, as shown in the Section 5 a modification taking into account the changed enthalpy related to cluster-defect interaction is required to provide an accurate model that is consistent with strength and microstructure data. In fact, it is well known that solutes and various types of defects interact and cluster together, including vacancy-solute clusters [75] and dislocation-solute clusters [76, 77], leading to a reduction of overall grain-boundary Gibbs free energy and a stabilization of ultrafine-grained microstructures [8, 36-38]. Thus this model modification is justifiable and required.

The interaction between dislocations and solute can be described by thermodynamic models, incorporating enthalpy and entropy terms [20, 24]. In line with this, in our strength model modification we introduced a new parameter, $\Delta H_{\text{A-B-dis}}$, which for the present alloy was determined by fitting to be 50±5 kJ/mole. (At present we are not considering the entropy related to this interaction; it is thought that at room temperature this effect is negligible.) This $\Delta H_{\text{Cu-Mg-dis}}$ accounts for the different fractions of Cu-Mg clusters in Al matrix, solute atoms segregated to dislocations and Cu-Mg clusters segregated to dislocations. The proportions of each part may be adjustable, because the amount of atoms/clusters segregated to dislocations or grain boundaries can be different between HPT samples subjected to different rotations (see Fig. 8 and Fig. 9). We avoid focusing on the proportion of $\Delta H_{\text{Cu-Mg-dis}}$ correlated to the various types of solute-defect interactions and clustering, and instead adjust $\Delta H_{\text{Cu-Mg-dis}}$ to obtain a single averaged $\Delta H_{\text{Cu-Mg-dis}}$ (see also [75-77] and [36-38]). Fig. 11 shows this works well providing the HPT is conducted for one rotation or more. Apparently the one rotation of HPT is sufficient to reach conditions in which relative proportions of the different solute-defect interactions and their contribution to $\Delta H_{\text{Cu-Mg-dis}}$ are stationary on further deformation.

We believe that the reduced strength at very low deformations (less than 1 HPT turn) is due to the mobility of solute atoms (which is enhanced by deformation induced vacancy generation) and the movement of dislocations being too limited to form substantial dislocation-cluster complexes.

The $\Delta H_{\text{Cu-Mg-dis}}$ value of 50 kJ/mole is larger than an enthalpy determined from the 5×5×1 and 6×6×1 supercell calculation in a GPB structure [78], suggesting that the Cu-Mg-defect cluster complexes are quite stable. In fact with this value of $\Delta H_{\text{Cu-Mg-dis}}$, the defect-cluster complexes in the SPD materials can be more stable than some of the intermediate precipitates, and the solute atoms captured in the cluster-defect complexes will not transform to GPB zones or intermediate precipitates on ageing, unless changes elsewhere in the material (away from the cluster-defect complexes) changes this local situation. On continuous heating these cluster-defect complexes would be more stable than the co-clusters present in solution treated and aged Al-Cu-Mg alloys. To validate this we performed differential scanning calorimetry on the HPT processed alloys at heating rate 10 °C/min. This confirmed that whilst for similar Al-Cu-Mg alloys in solution treated and room temperature aged condition a strong endothermic effect due to co-cluster dissolution occurs from about 140 °C with an endothermic maximum at 220 °C [47], the present (solution treated, RT aged, HPT processed and subsequently RT aged) samples no endothermic effect is detected in this temperature range. The present analysis of cluster-defect complexes suggests that only dislocation movement and annihilation at elevated temperature and/or the formation of stable phases would be able to cause the dissolution of these cluster-defect complexes.

Our understanding of cluster segregation to grain boundaries and dislocations rests on APT data and the statistical analysis of that data. When APT is performed on the ultrafine-grained Al-Cu-Mg alloy, a wide range of cluster types and compositions (Table 1) are generally detected, which may seem at variance with the present model. However, the APT data is

based on statistical analysis of the locations of atoms that are detected at a detection rate of about 50~55% [24, 26], and hence many of the the two-atom or four-atom types (based on A-B dimers) that are illustrated in Fig.1(a) cannot be identified individually. For each dimer present in the alloy, the APT experiment with cluster identification algorithm can provide 4 outcomes: if both atoms in the dimer are detected the result can be the detection of the A-B dimer, if only A is detected the outcome is a single dissolved atom A, if only B is detected the outcome is a single dissolved atom B, and if both atoms are go undetected then nothing is detected. For 4 atoms clusters similarly a range of possible outcomes can occur. This leads both to an underestimate of the amount of clusters as well as an overestimate of the variety of cluster compositions [24]. The APT data does confirm that the Cu:Mg ratio of atoms in the cluster is very close to unity, which is consistent with the model.

7. Conclusions

A physically-based strengthening model for ternary and higher order work hardened alloys is presented. It includes short-range order and modulus hardening due to clusters, and strengthening due to dissolved atoms, grain boundaries and dislocations. In a further expansion it also takes account of complex solute-defect clusters through the definition of an averaged enthalpy of formation of the solute-defect clusters, $\Delta H_{\text{A-B-dis}}$.

The model is applied to estimate the strength of an Al-Cu-Mg alloy after high pressure torsion. The expanded model fits very well to the strength data obtained for the Al-Cu-Mg alloy subjected to different rotations of high pressure torsion. The analysis indicates:

- APT shows that both before and after HPT the alloy contains a high density of clusters, which are predominantly of the Cu-Mg co-cluster type. The model indicates that short range order due to these clusters is the dominant strengthening mechanism. The interactions

between dislocations and Cu-Mg clusters leading to complex solute-defect clusters further increase the strength and reduce the free energy of Al matrix.

- Through fitting $\Delta H_{\text{Cu-Mg-dis}}$ is determined to be 50±5 kJ/mole, which suggests the solute-defect clusters are more stable than some of the intermediate precipitates such as GPB zones.

- XRD line broadening analysis reveals the increase in dislocation density in the HPT processed samples. This provides a significant strengthening (about 10% of the strength of HPT processed samples).

- XRD line broadening analysis indicates HPT produces a refinement of domain size to ~50 nm for HPT processing of 1 to 16 turns. TEM shows the grain size is about 3 times the domain size. The grain size strengthening is the 3rd most potent strengthening mechanism in these HPT processed ternary Al-Cu-Mg alloys.

Reference

[1] Zhilyaev AP, Langdon TG. Progress in Materials Science 2008;53:893.
[2] Zhang J, Gao N, Starink MJ. Materials Science and Engineering: A 2010;527:3472.
[3] Vafaei R, Toroghinejad MR, Pippan R. Materials Science and Engineering: A 2012;536:73.
[4] Zhao YH, Liao XZ, Jin Z, Valiev RZ, Zhu YT. Acta Materialia 2004;52:4589.
[5] Ghosh KS, Gao N, Starink MJ. Materials Science and Engineering: A 2012;552:164.
[6] Chinh NQ, Gubicza J, Czeppe T, Lendvai J, Xu C, Valiev RZ, Langdon TG. Materials Science and Engineering: A 2009;516:248.
[7] Duan Z, Liao X, Kawasaki M, Figueiredo R, Langdon T. Journal of Materials Science 2010;45:4621.
[8] Chookajorn T, Murdoch HA, Schuh CA. Science 2012;337:951.
[9] Deschamps A, De Geuser F, Horita Z, Lee S, Renou G. Acta Materialia 2014;66:105.
[10] Xu C, Furukawa M, Horita Z, Langdon TG. Acta Materialia 2003;51:6139.
[11] Ashby MF. Philosophical Magazine 1970;21:399
[12] Hansen N. Acta Metallurgica 1977;25:863.
[13] Estrin Y, Mecking H. Acta Metallurgica 1984;32:57.
[14] Estrin Y, Molotnikov A, Davies CHJ, Lapovok R. Journal of the Mechanics and Physics of Solids 2008;56:1186.
[15] Starink MJ, Qiao XG, Zhang J, Gao N. Acta Materialia 2009;57:5796.
[16] Qiao XG, Gao N, Starink MJ. Philosophical Magazine 2011;92:446.
[17] Valiev RZ, Islamgaliev RK, Alexandrov IV. Progress in Materials Science 2000;45:103.
[18] Ringer SP, Hono K, Sakurai T, Polmear IJ. Scripta Materialia 1997;36:517.
[19] Starink MJ, Gao N, Yan JL. Materials Science and Engineering A 2004;387-389:222.
[20] Starink MJ, Wang SC. Acta Materialia 2009;57:2376.
[21] Marceau RKW, Sha G, Ferragut R, Dupasquier A, Ringer SP. Acta Materialia 2010;58:4923.
[22] Murayama M, Hono K. Acta Materialia 1999;47:1537.
[23] Kim J, Daniel Marioara C, Holmestad R, Kobayashi E, Sato T. Materials Science and Engineering: A 2013;560:154.
[24] Starink MJ, Cao LF, Rometsch PA. Acta Materialia 2012;60:4194.

[25] Liddicoat PV, Liao X-Z, Zhao Y, Zhu Y, Murashkin MY, Lavernia EJ, Valiev RZ, Ringer SP. Nat Commun 2010;1:63.
[26] Sha G, Tugcu K, Liao XZ, Trimby PW, Murashkin MY, Valiev RZ, Ringer SP. Acta Materialia 2014;63:169.
[27] Nurislamova G, Sauvage X, Murashkin M, Islamgaliev R, Valiev R. Philosophical Magazine Letters 2008;88:459.
[28] Sha G, Yao L, Liao X, Ringer SP, Chao Duan Z, Langdon TG. Ultramicroscopy 2011;111:500.
[29] Valiev RZ, Enikeev NA, Murashkin MY, Kazykhanov VU, Sauvage X. Scripta Materialia 2010;63:949.
[30] Liu Z, Chen X, Han X, Gu Y. Materials Science and Engineering: A 2010;527:4300.
[31] Liu Z, Bai S, Zhou X, Gu Y. Materials Science and Engineering: A 2011;528:2217.
[32] Huang W, Liu Z, Lin M, Zhou X, Zhao L, Ning A, Zeng S. Materials Science and Engineering: A 2012;546:26.
[33] Murayama M, Horita Z, Hono K. Acta Materialia 2001;49:21.
[34] Lechner W, Puff W, Mingler B, Zehetbauer MJ, Würschum R. Scripta Materialia 2009;61:383.
[35] Weissmüller J. Nanostructured Materials 1993;3:261.
[36] Kirchheim R. Acta Materialia 2002;50:413.
[37] Kirchheim R. Acta Materialia 2007;55:5129.
[38] Kirchheim R. Acta Materialia 2007;55:5139.
[39] Zhang T-Y, Ren H. Acta Materialia 2013;61:477.
[40] Wang SC, Zhu Z, Starink MJ. Journal of Microscopy 2005;217:174.
[41] Starink MJ, Wang SC. Acta Materialia 2003;51:5131.
[42] Zhang J, Gao N, Starink MJ. Materials Science and Engineering: A 2011;528:2581.
[43] Starink MJ. International Journal of Materials Research 2012;103:942.
[44] Starink MJ, Deschamps A, Wang SC. Scripta Materialia 2008;58:377.
[45] Starink MJ, Cheng X, Yang S. Acta Materialia 2013;61:183.
[46] Gao H, Huang Y, Nix WD, Hutchinson JW. Journal of the Mechanics and Physics of Solids 1999;47:1239.
[47] Starink MJ, Gao N, Davin L, Yan J, Cerezo A. Philosophical Magazine 2005;85:1395.
[48] Shercliff HR, Ashby MF. Acta Metallurgica et Materialia 1990;38:1789.
[49] Ryen Ø, Holmedal B, Nijs O, Nes E, Sjölander E, Ekström H-E. Metallurgical and Materials Transactions A 2006;37:1999.
[50] Flinn PA. Acta Metallurgica 1958;6:631.
[51] Gomiero P, Brechet Y, Louchet F, Tourabi A, Wack B. Acta Metallurgica et Materialia 1992;40:857.
[52] Smithells CJ, Brandes EA, Brook GB. Smithells' metals reference book: Butterworth-Heinemann, 1992.
[53] Dunstan DJ, Bushby AJ. International Journal of Plasticity 2013;40:152.
[54] Dunstan DJ, Bushby AJ. International Journal of Plasticity 2014;53:56.
[55] Korte S, Clegg WJ. Philosophical Magazine 2010;91:1150.
[56] Taylor GI. Proceedings of the Royal Society of London. Series A, Containing Papers of a Mathematical and Physical Character 1934;145:388.
[57] Hall EO. Proceedings of the Physical Society. Section B 1951;64:747.
[58] Institute of M, Faraday S. Symposium on internal stresses in metals and alloys. London, 1948.
[59] Brooks H. American Society for Metals, Metals Park, OH 1952:20.
[60] Meyers MA, Mishra A, Benson DJ. Progress in Materials Science 2006;51:427.
[61] Zhang J, Starink MJ, Gao N, Zhou W. Materials Science Forum 2010:809.
[62] Zhang P, Li SX, Zhang ZF. Materials Science and Engineering: A 2011;529:62.
[63] Qiao XG, Starink MJ, Gao N. Acta Materialia 2010;58:3690.
[64] McCusker LB, Von Dreele RB, Cox DE, Louer D, Scardi P. Journal of Applied Crystallography 1999;32:36.
[65] Sha G, Cerezo A. Acta Materialia 2004;52:4503.
[66] Sha G, Marceau RKW, Gao X, Muddle BC, Ringer SP. Acta Materialia 2011;59:1659.
[67] Ungár T. Scripta Materialia 2004;51:777.
[68] Williamson GK, Smallman RE. Philosophical Magazine 1956;1:34.
[69] Čížek J, Janeček M, Srba O, Kužel R, Barnovská Z, Procházka I, Dobatkin S. Acta Materialia 2011;59:2322.
[70] Ferrari M, Lutterotti L. Journal of Applied Physics 1994;76:7246.
[71] Lutterotti L, Gialanella S. Acta Materialia 1998;46:101.
[72] Lutterotti L, Matthies S, Wenk H. MAUD (material analysis using diffraction): a user friendly Java program for Rietveld texture analysis and more. Proceeding of the Twelfth International Conference on Textures of Materials (ICOTOM-12), vol. 1: NRC Press Ottawa, Canada, 1999. p.1599.
[73] Young RA, Wiles DB. Journal of Applied Crystallography 1982;15:430.

[74] Caglioti G, Paoletti A, Ricci FP. Nuclear Instruments 1958;3:223.
[75] Aust KT, Hanneman RE, Niessen P, Westbrook JH. Acta Metallurgica 1968;16:291.
[76] Cottrell A. Effect of solute atoms on the behavior of dislocations. Report of a Conference on Strength of Solids, 1948. p.30.
[77] Suzuki H. Science reports of the Research Institutes, Tohoku University. Ser. A, Physics, chemistry and metallurgy 1952;4.
[78] Kovarik L, Court SA, Fraser HL, Mills MJ. Acta Materialia 2008;56:4804.

Table 1 Number densities of detected clusters in Al-4.3Cu-1.5Mg-0.08Si wt.% processed by ¼ rotation and 5 rotations of HPT at room temperature.

HPT rotations	No. density $\times 10^{26} m^{-3}$				Alloy composition (at.%)	
	All	Mg-Cu	Cu-Cu	Mg-Mg	Mg	Cu
1/4r	1.90	1.06	0.34	0.42	1.67	1.69
5r	1.99	1.07	0.37	0.45	1.71	1.49

Table 2 Parameter values used in the model.

Parameters	Value	Refs.
M	2.6	[40, 41]
$\Delta\tau_0$	10 MPa	[40, 41]
α_1	0.3	[16]
G	26 GPa	[16]
k_{Cu}	10 MPa/at%Cu	[40, 47-49]
k_{Mg}	6 MPa/at%Mg	[47-49, 75]
n	1	[47-49, 75]
y_{Cu}	1.8 at.%	See text and [20]
y_{Mg}	1.8 at.%	See text and [20]
b	0.286 nm	[40, 41]
a_2	2	[15]
C	3	[16, 42, 60-63]

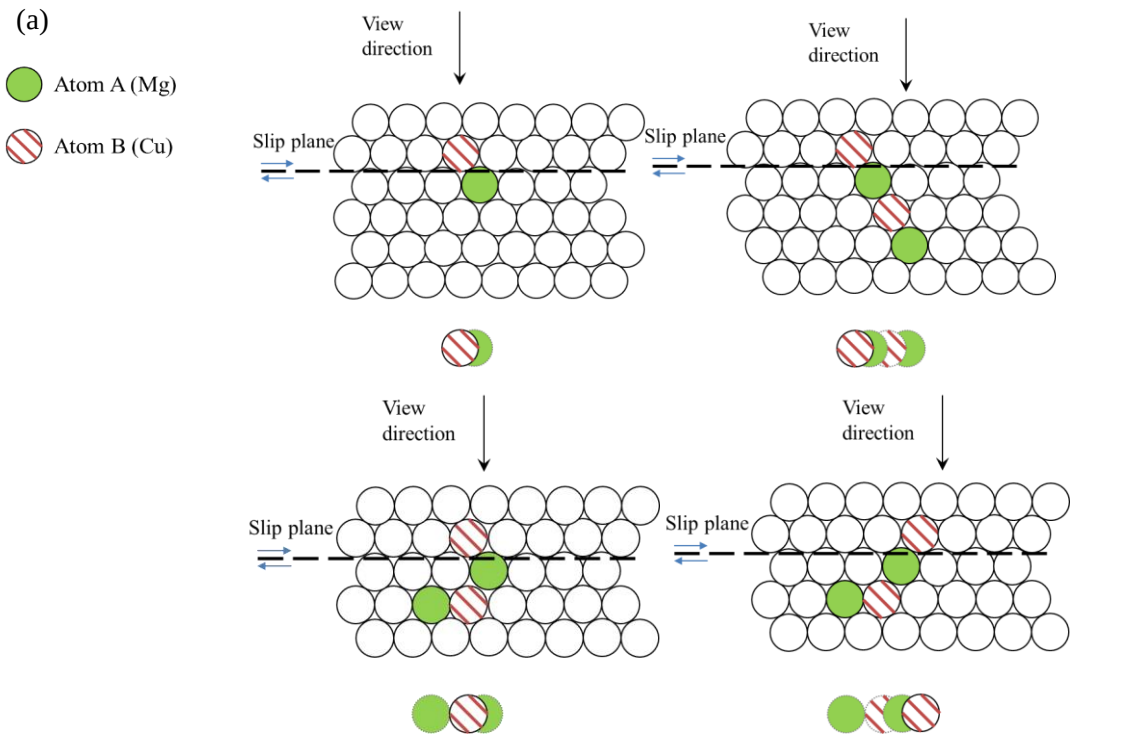
(a)
Atom A (Mg)
Atom B (Cu)
View direction
Slip plane
View direction
Slip plane
View direction
Slip plane
View direction
Slip plane

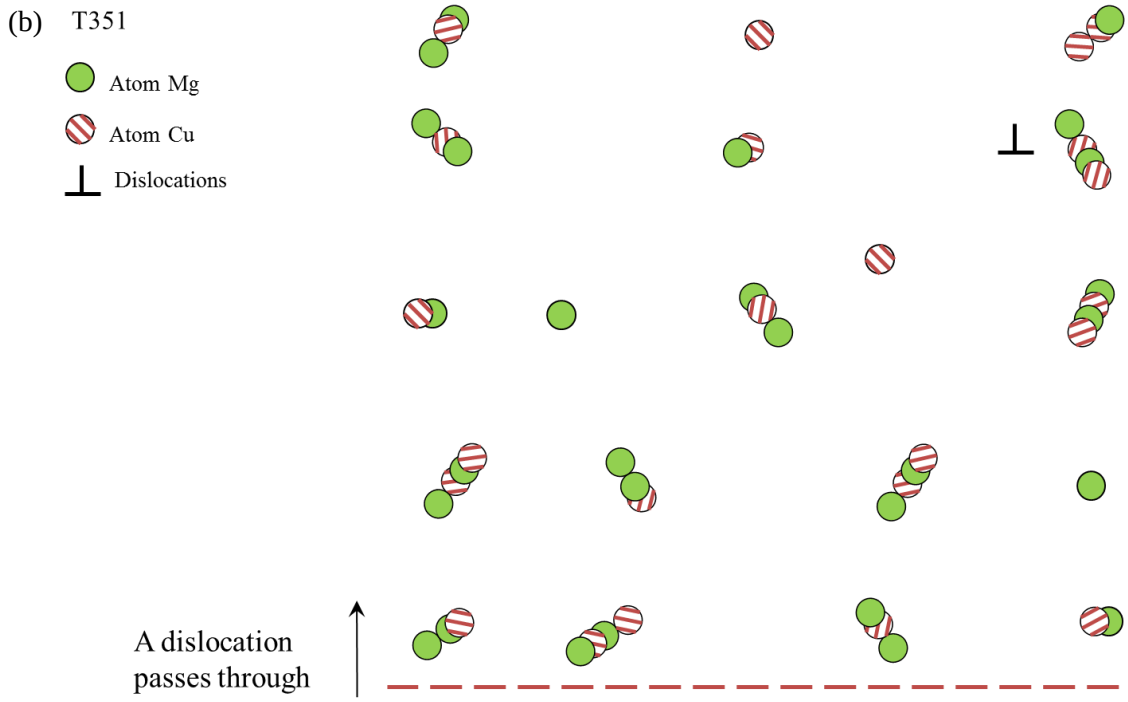
(b) T351
Atom Mg
Atom Cu
Dislocations
A dislocation passes through

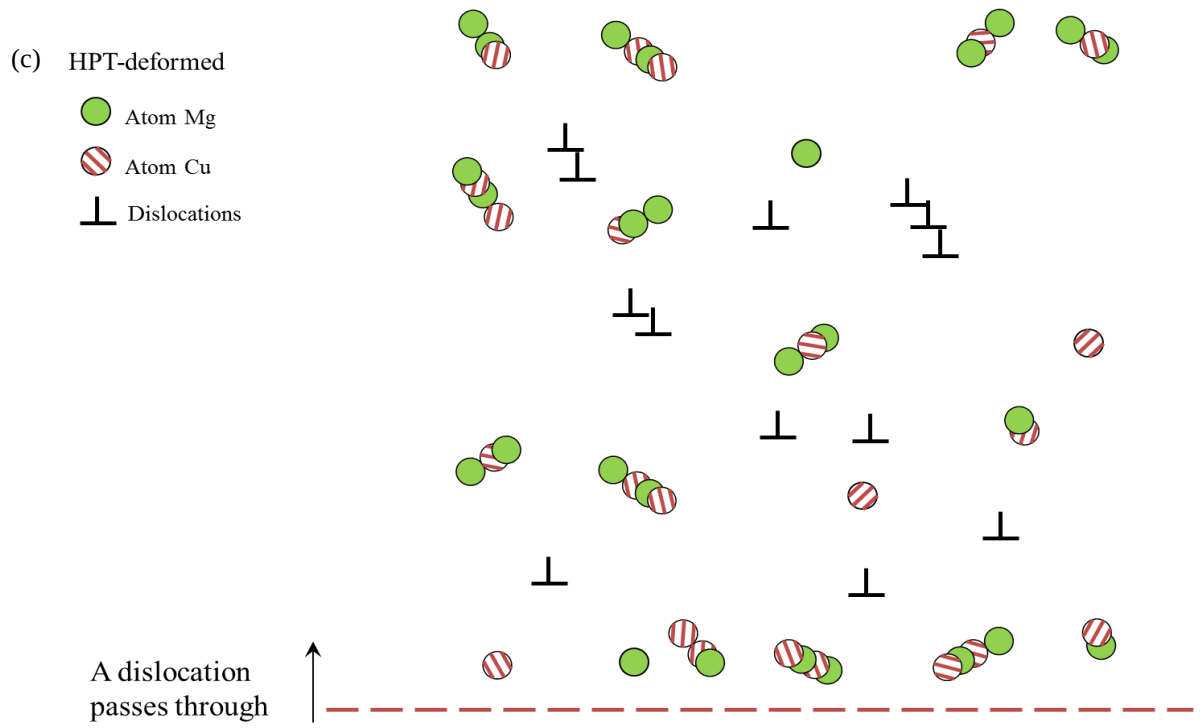

Fig.1 (a) Schematic illustrations of (a) co-clusters and a slip plane in a (111) plane of an FCC lattice with a 2-atom co-cluster (left) and 4-atom co-cluster (right), the view direction is the direction employed in (b) and (c); (b) simplified view of a moving dislocation with clusters, solutes and (a low density of) dislocation intersecting the slip plane in its path (illustrating the situation in an Al-Cu-Mg alloy with limited pre deformation); (c) simplified view of a moving dislocation with clusters, solutes and a high density of dislocations intersecting the slip plane in its path (resembling a SPD processed Al-Cu-Mg alloy).

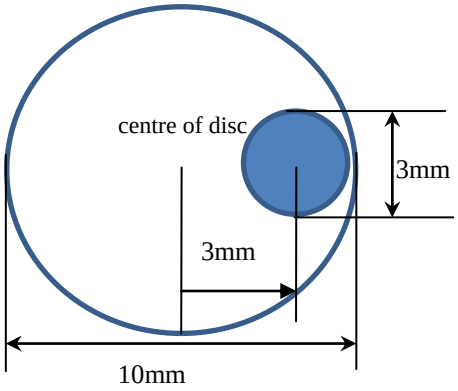

Fig.2 TEM sample (blue) punched from the HPT processed disc.

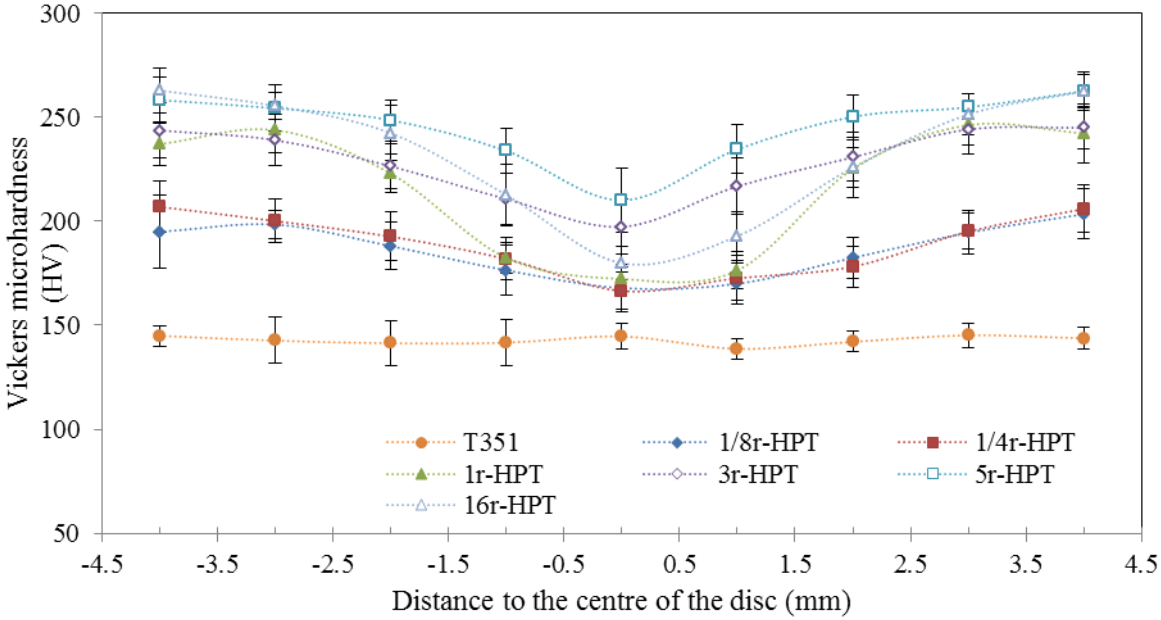

Fig. 3 Microhardness distribution versus distance to the centre of HPT discs at various rotations at ambient temperature.

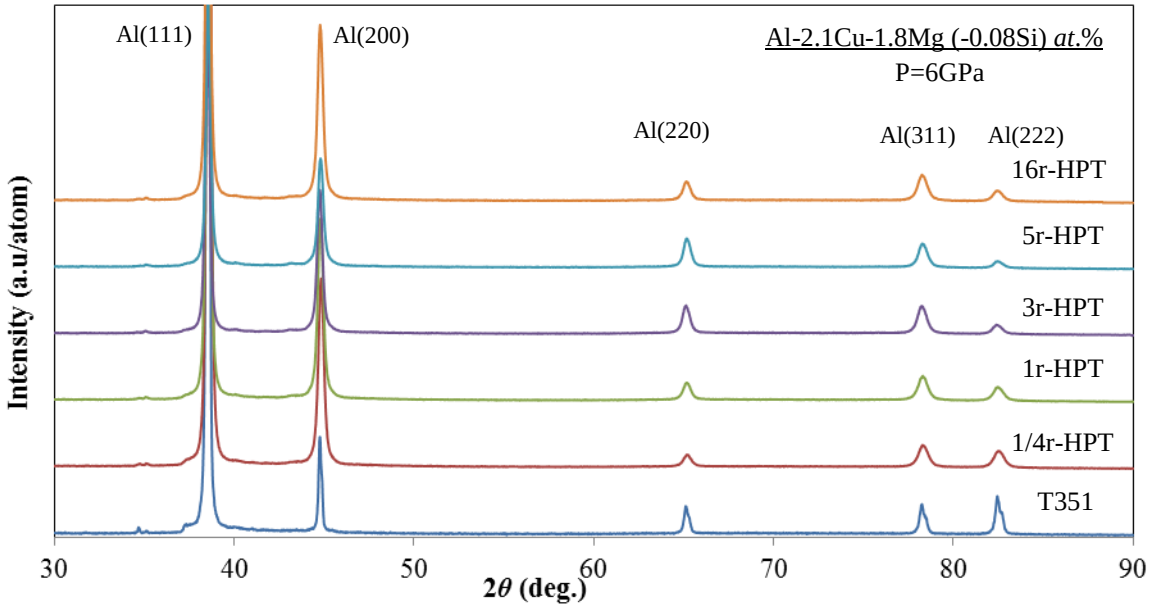

Fig. 4 The X-ray diffraction patterns of the alloy deformed by HPT for ¼, 1, 3, 5 and 16 rotations.

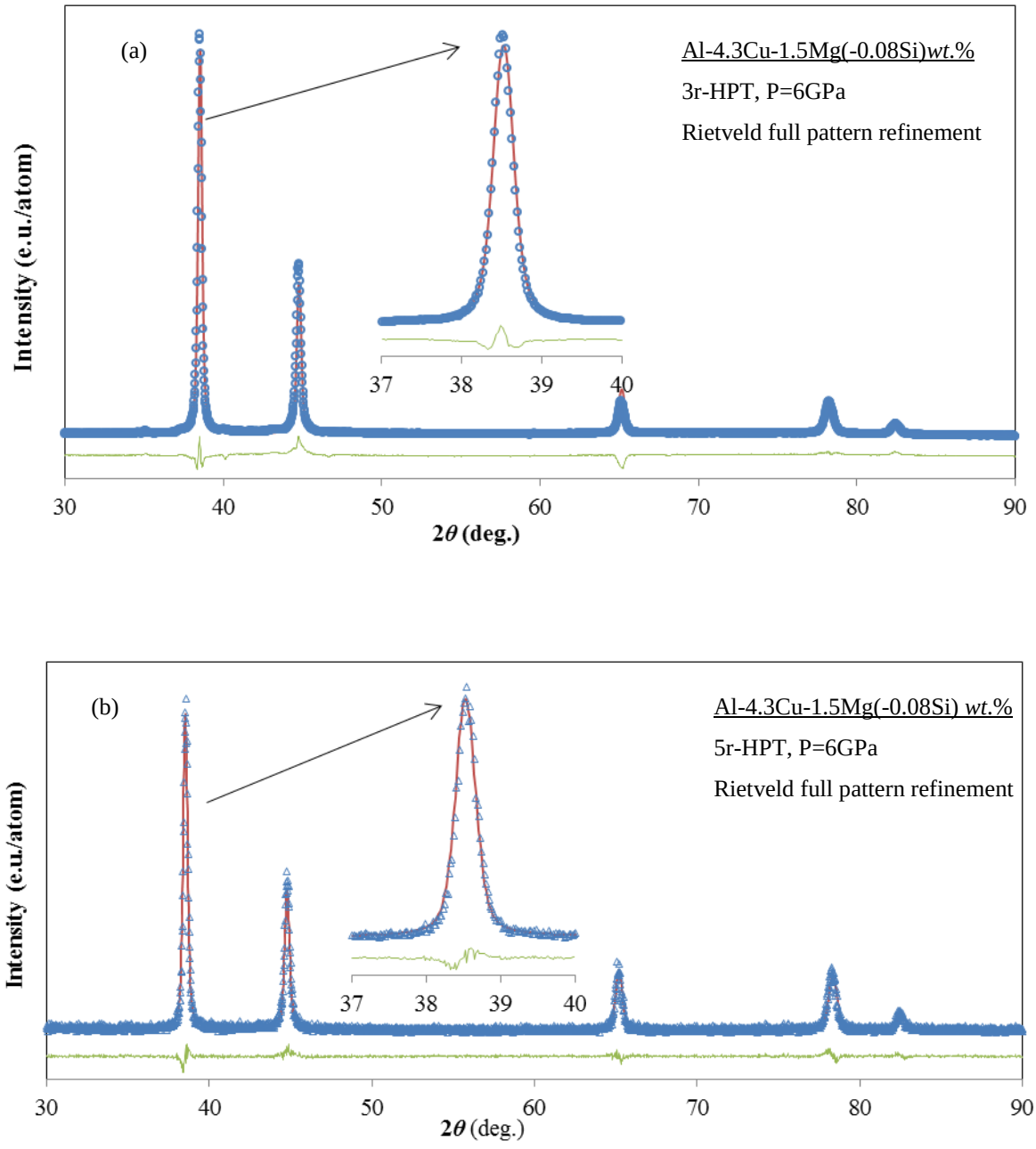

Fig. 5 Rietveld analysis fits for X-ray diffraction patterns of 3r-HPT (a) and 5r-HPT sample (b). Experimental data of 3r-HPT and 5r-HPT are shown symbols; and the refined simulated patterns are shown as continuous solid line. The difference between experimental data and fitted simulated pattern is shown as continuous line under each diffraction pattern.

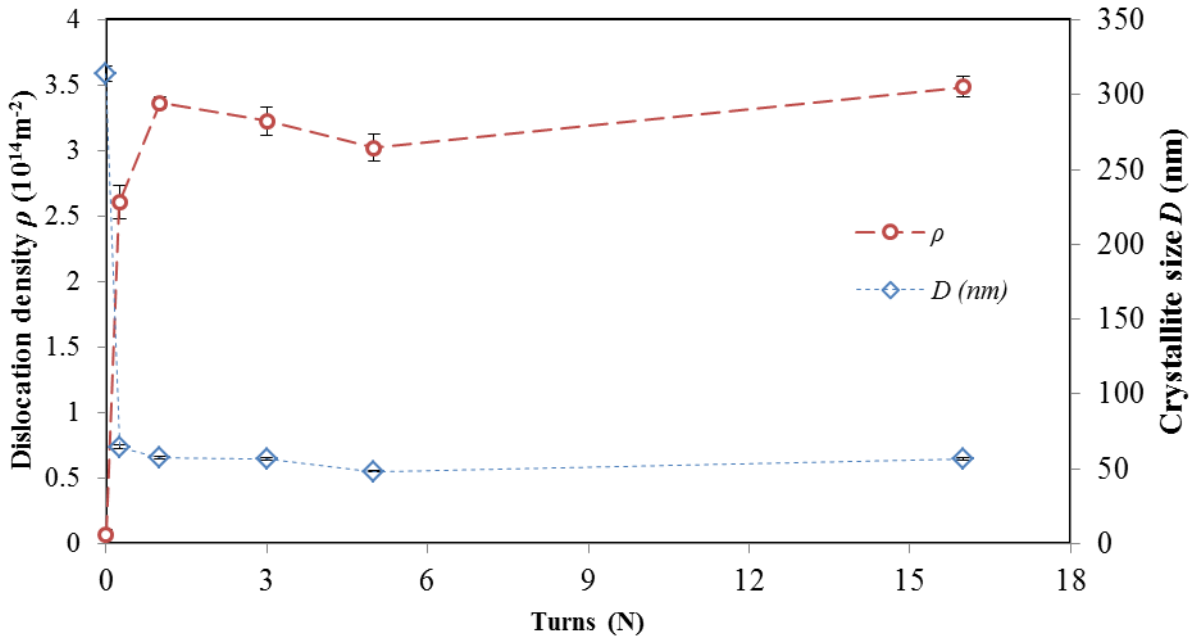

Fig. 6 The crystallite size (coherently scattering domains) and average dislocation density determined by Rietveld full pattern refinement plotted as a function of the number of HPT rotations.

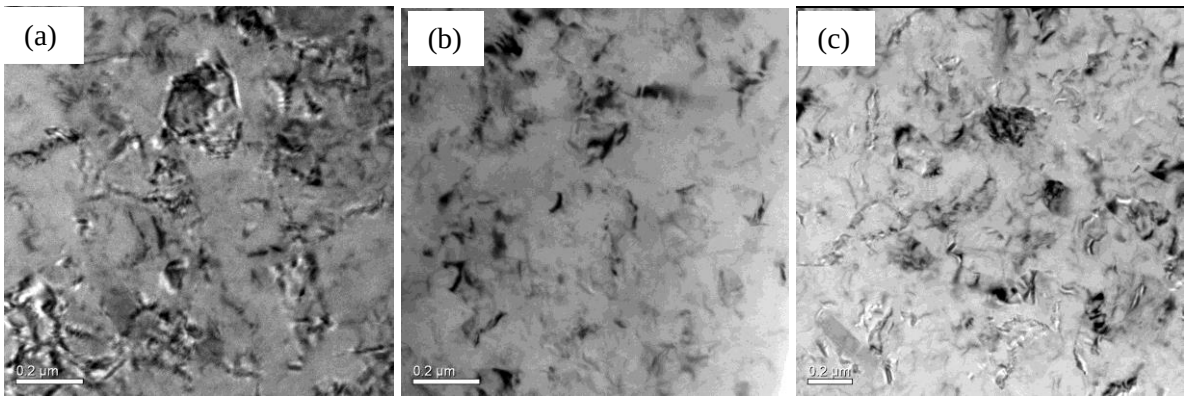

Fig. 7 TEM bright field images of (a) 1/4r-HPT, (b) 1r-HPT and (c) 5r-HPT samples

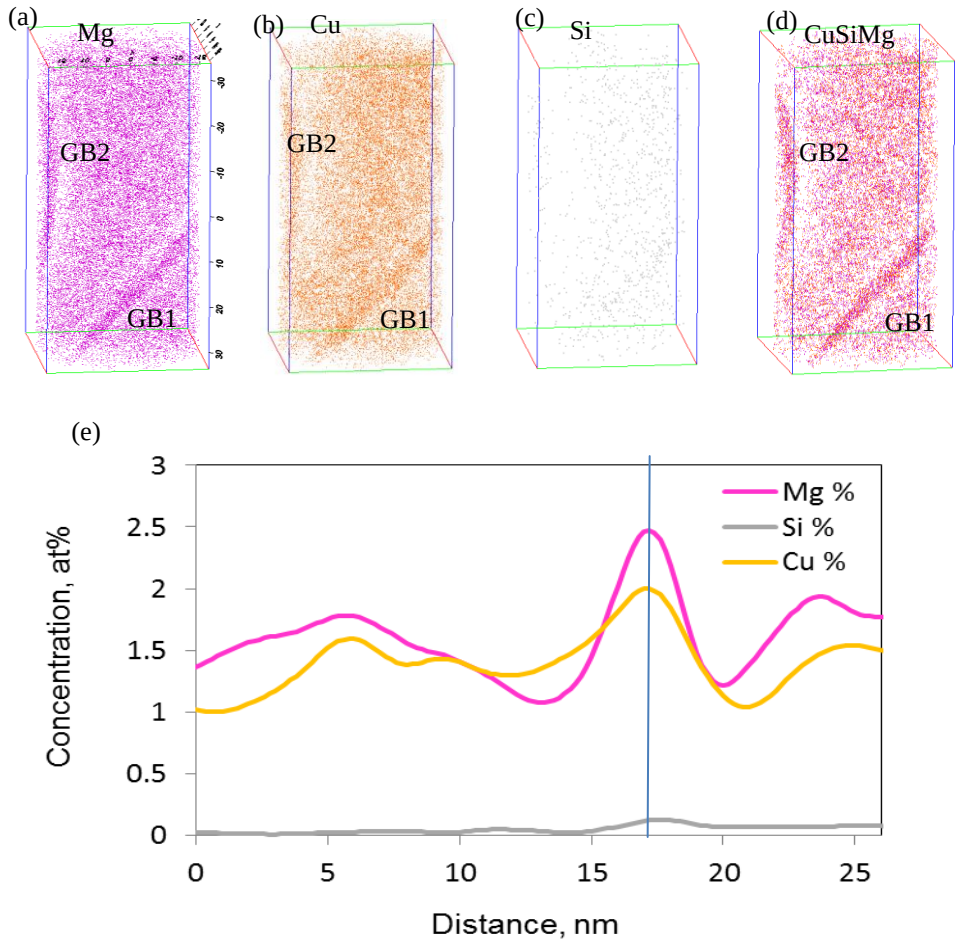

Fig. 8 Single-element atom maps of one 1/4r-HPT Al-Cu-Mg sample (a) Mg map, (b) Cu map, (c) Si map and (d) CuSiMg map; (e) composition profiles of GB1 measured using a selection box with the z-axis parallel to grain boundary plane normal.

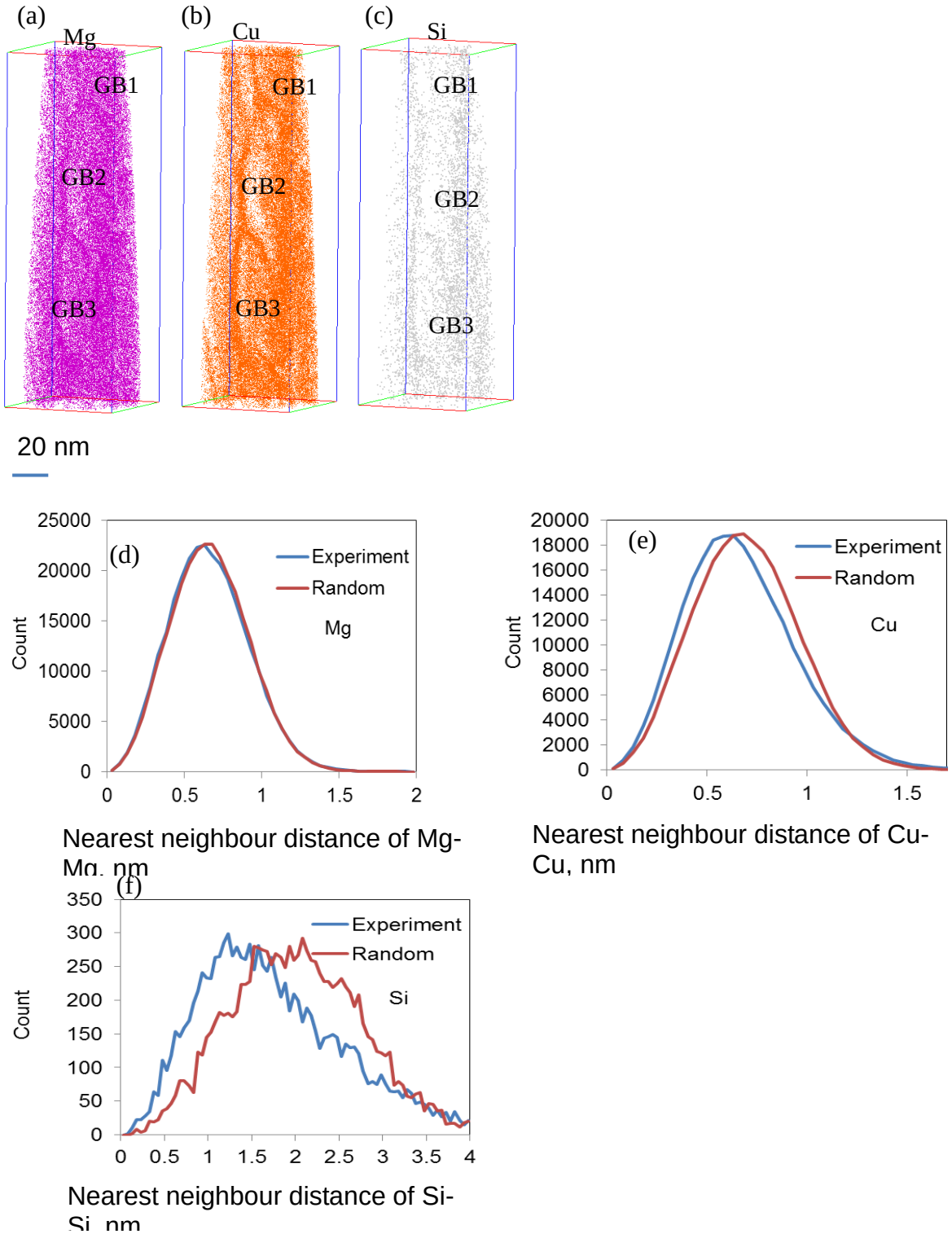

Fig. 9 Single-element atom maps of one 5r-HPT Al-Cu-Mg sample (a) Mg map, (b) Cu map, (c) Si map; (d) (e) (f) near-neighbour distribution of Mg, Cu and Si, respectively.

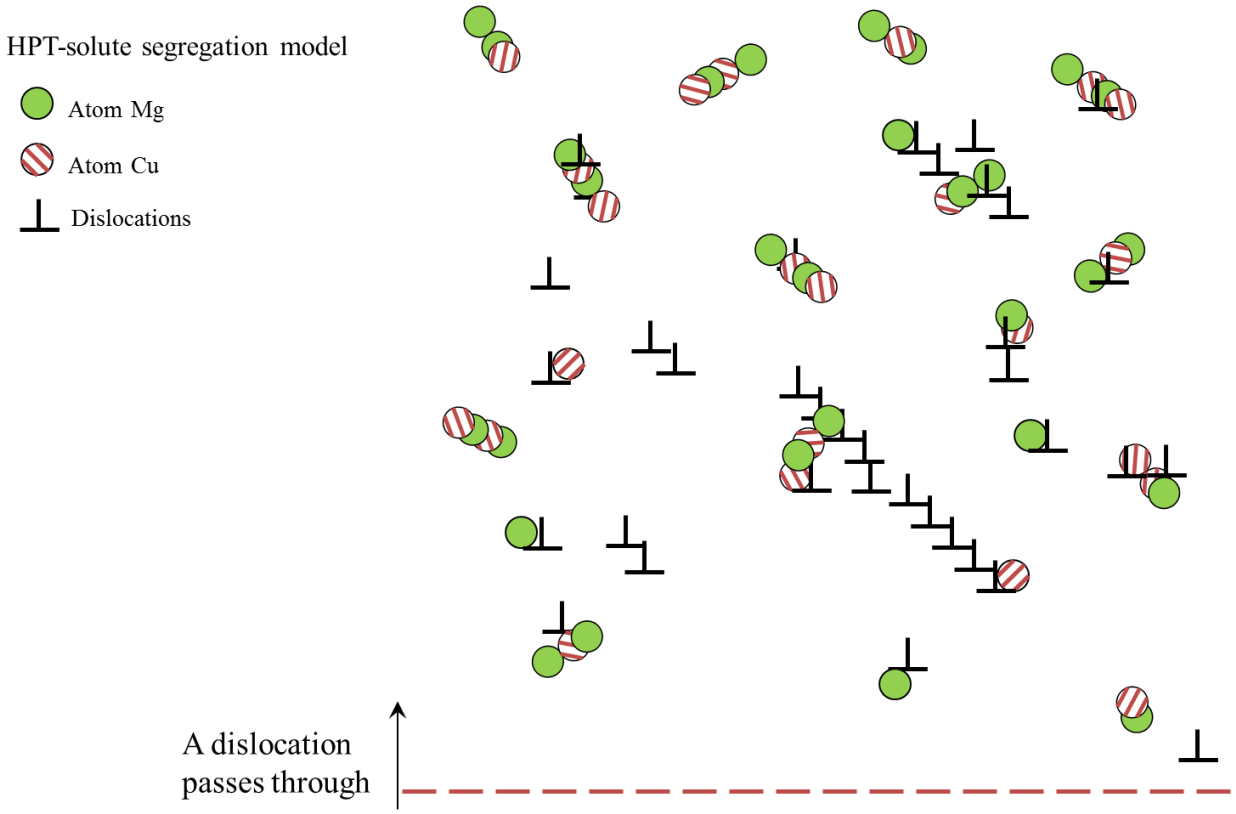

Fig. 10 Schematic illustration of a moving dislocation with clusters, solutes, dislocations and dislocation-cluster complexes intersecting the slip plane in its path (illustrating the situation in an SPD processed Al-Cu-Mg alloy).

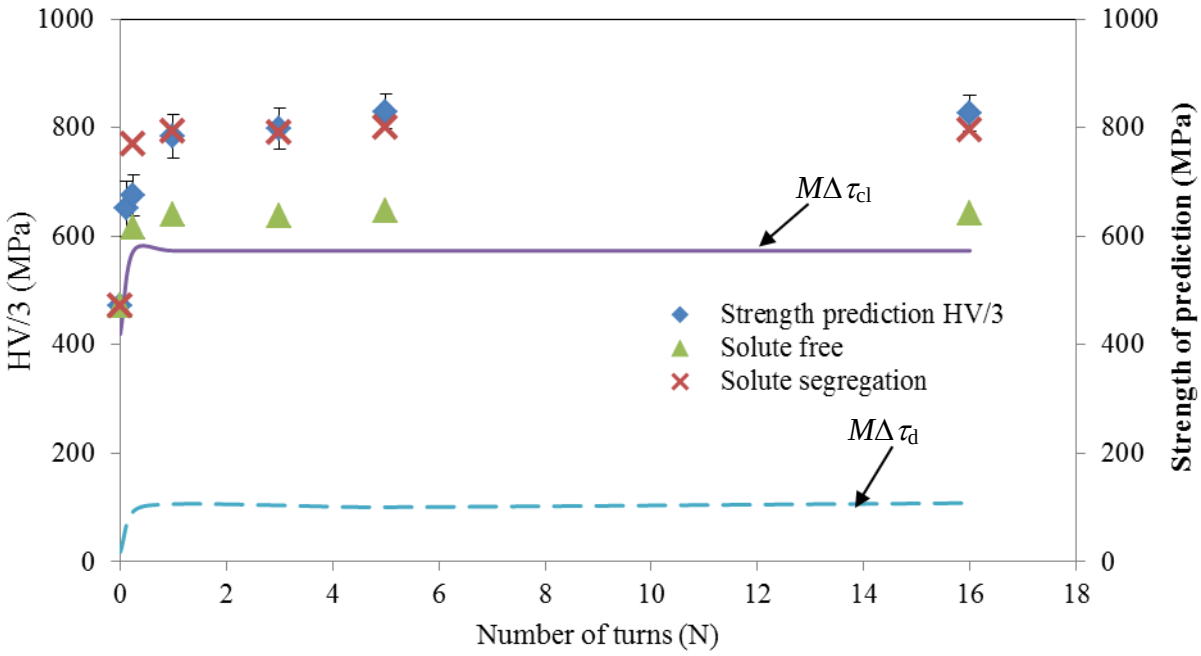

Fig. 11 HV/3 (♦) compared with model predictions of strength using 2 model variants: the case for solutes and clusters being separated from defects (grain boundaries and dislocations) (▲) and for clusters being associated with defects providing an enhanced strengthening effect (×). Also plotted are the two main strengthening effects in the HPT processed materials due to cluster-defect complexes ($M\Delta\tau_{cl}$) and strengthening due to dislocations ($M\Delta\tau_{d}$).